Thermal Science and Engineering Progress 37 (2023) 101586

Contents lists available at ScienceDirect

Thermal Science and Engineering Progress

journal homepage: www.sciencedirect.com/journal/thermal-science-and-engineering-progress

An investigation of droplet impingement on a conical obstacle

Li Wang, Xin Wang, Yuying Yan *

Faculty of Engineering, University of Nottingham, Nottingham NG7 2RD, UK

ARTICLE INFO

Keywords:
Droplet impingement
Conical obstacle
Wettability
Leidenfrost phenomenon
Lattice Boltzmann method

ABSTRACT

Droplet impingement has been intensively studied in recent years due to its wide range of applications. In the present study, a multi-component multiphase Lattice Boltzmann model is adopted to study the droplet impingement on conical obstacles. A modified non-slip bounce-back boundary condition is applied to simulate the wetting of droplets on the hypotenuse of the cones. The model is validated for its capability to achieve accurate results, and then the effect of gravity, as well as surface wettability and surface temperature is investigated. Three different droplet behaviours are observed upon the impingement, respectively, namely, rebounding and wrapping the vertex, sliding down against the hypotenuse, and sliding down levitated. The increase in gravity and hydrophilicity reduces the chance of the droplet wrapping the vertex, while the increase in hydrophobicity and temperature increases the chance of the droplet sliding down levitated. A detailed snapshot is presented to indicate the influence of surface wettability on the droplet's movement and morphology. In general, as the surface becomes more hydrophobic, the droplet gains a larger overall velocity, but the deformation also influences the movement of the droplet. The droplet in the Leidenfrost stage is also investigated, and the relationship between the Jakob number and droplet velocity and temperature distribution is obtained. This study aims to reveal the characteristics of the impingement between a droplet and a conical obstacle and provide fundamental support to related engineering applications such as spray cooling.

Introduction

Droplet impingement is receiving a high volume of attention due to its wide applications, such as inkjet printing [1,2], spray cooling [3,4], surface coating [5], and oil recovery [6]. The behaviour of droplets upon impingement depends on many factors, such as the liquid property, droplet volume, impacting velocity, and temperature. Cheng et al. [7] studied the effect of impact velocity, surface tension, initial droplet radius, equilibrium contact angle, and liquid viscosity on droplet spreading and found that the droplet spreading rate will increase with the increasing impact velocity, surface tension, and initial radius, or decreasing equilibrium contact angle and liquid viscosity. Lin et al. [8] experimentally studied the effect of liquid viscosity, impact velocity, and surface wettability on the impact dynamics, and different droplet behaviours, like depositing, rebounding, and splashing are observed by tuning these factors. Liu et al. [9] studied the influence of Weber number and surface temperature on droplet impingement. Both non-Leidenfrost and Leidenfrost droplets are investigated, and the relationship between temperature change and time, affected by the impact dynamics is given.

As the impingement happens in various kinds of scenarios, the droplet does not always impinge on flat surfaces but could impinge on surfaces with complex structures. Many researchers have used both experimental and numerical methods to study droplet impingement on surfaces with different structures and found that surface geometry can affect impingement behaviours dramatically. Some of the most intensively investigated geometries are flat surfaces [10,11] and inclined walls [12,13], pillars [14,15], spheres [16–18], cylinders [19], and rectangular obstacles [20]. Our previous study also involves droplet impingement on surfaces with microstructures [21,22]. As one of the most representative geometric shapes, droplet impingement on conical obstacles is relatively less studied, yet is gaining interest from researchers. The pointy shape of cones makes the droplet more likely to rupture while impinging, resulting in a larger contact area as the droplet breaks into many smaller ones rolling downing the cone, hence a better heat transfer efficiency can be achieved. Also, as the vertical momentum of the droplet is redirected horizontally by the cone, the way the droplet interact with the surface would be totally different from that on a flat surface. Both those characteristics are of great benefit in cases such as spray cooling. Shen et al. [23] used both experimental and numerical means to investigate the impingement of a droplet on dome convex superhydrophobic surfaces, and pointed out that compared to a flat

* Corresponding author.
E-mail address: yuying.yan@nottingham.ac.uk (Y. Yan).

https://doi.org/10.1016/j.tsep.2022.101586
Received 7 October 2022; Received in revised form 26 November 2022; Accepted 28 November 2022
Available online 5 December 2022

Nomenclature

We	Weber number
Ja	Jakob number
Re	Reynold number
Bo	Bond number
t^*	Dimensionless time
δt	Time interval
T 0-a	Temperature 0-b0-c
l 0-d	Length 0-e
f_σ 0-f	Distribution function for stream of the σ_{th} component0-g
f_σ^{eq} 0-h0-i	Equilibrium distribution for stream of the σ_{th} component0-j component0-k
g_σ 0-l	Distribution function for temperature of the σ_{th} component0-mcomponent0-n
g_σ^{eq} 0-o	Equilibrium distribution function for temperature of the σ_{th} component0-pcomponent0-q
e_i 0-r	Lattice particle's microscopic speed 0-s
c 0-t	Reference lattice velocity
u 0-u	Velocity 0-v
U 0-w	Real velocity 0-x
p 0-y	Pressure 0-z
c_p 0-aa	Thermal specific heat at constant pressure 0-bb
c_v *0-cc*	Thermal specific heat at constant volume 0-dd
H' *0-ee*	Droplet initial height 0-ff
d 0-gg	Droplet diameter 0-hh
g	Gravity acceleration 0-ii
F	Interaction force 0-jj
G 0-kk	Coefficient for interaction forces
R	Ideal gas constant
h_{lv} *0-ll*	Liquid-vapor latent heat

Greek symbols

σ 0-mm	Surface tension 0-nn
ω_i	Weight coefficients
α 0-qq	Thermal diffusivity 0-rr
β	Weighting factor
τ 0-ss	Relaxation time for stream field
τ_T 0-tt	Relaxation time for temperature field
ω_i 0-uu	Weight coefficients in *i* direction0-vv direction
ϕ 0-ww	Phase change source term
ρ 0-xx	Density 0-yy
λ *0-zz*	Heat conductivity 0-aaa
υ *0-bbb*	Kinetic viscosity 0-ccc
ψ, φ *0-ddd*	Effective mass of components
κ	Boundary force term tuning parameter

Super- and Sub- scripts

i 0-eee	Lattice direction
x	Lattice location
σ 0-fff	Liquid/vapor component
s 0-ggg	Solid phase
f	Fluid node
b	Boundary node
w	Wall boundary

superhydrophobic surface, the application of a convex surface can reduce the contact time of the droplet by 28.5 %. Also, the reduction in contact time is mainly determined by the retracting process. Liu et al. [24] studied the droplet impingement on a copper surface decorated with conical nanostructures. Pancake bouncing was observed upon the impingement, and the contact time was reduced by four times compared to the traditional complete rebound. Luo et al. [25] simulated the droplet impingement on a superhydrophobic cone, and found that the contact time can further be reduced to 54 % if the Weber number and the cone angle are chosen properly. A map of the phase diagram with Weber number and cone angle is also drawn. However, all those studies neglected the influence of temperature, and only impingement on superhydrophobic surfaces is studied, while the hydrophilic and neutral wetting surfaces are merely investigated. Besides, those studies focus more on how the contacting time can be reduced, while other behaviours of the droplet such as rupturing and sliding, are not investigated.

Compared to numerical methods, experimental methods encounter problems such as the micro size of the droplet and short timescale, as well as the fabrication of complex surfaces. Moreover, numerical simulation can show details of the flow field, such as velocity field, and temperature distribution and the relevant parameters can be adjusted freely [26]. In the aforementioned numerical research, the Volume of Fluid (VOF) method is used. However, computational fluid dynamics is very complicated in dealing with the liquid–air interface, and it takes a lot of computational resources to solve the pressure field and velocity field [27]. Compared to VOF, the Lattice Boltzmann method (LBM) can track the liquid–air interface automatically by incorporating intermolecular-level interactions [28]. Especially in cases where the liquid is not surrendered by just air, but by a mixture of non-condensable gas and vapour, as saturated liquid-saturated vapour interface does not have a sharp interface, but a finite thickness [29]. Furthermore, the contact angle doesn't need to be assumed constant, but adjustable by tuning the solid–liquid interaction force. LBM's intermolecular nature and mesoscopic scale make it more suitable to simulate multicomponent multiphase flows, and the ability of parallel computing and easy boundary treatment give it even more advantages. Many researchers have proved that LBM has satisfactory performance in simulating cases involving droplet impingement. Two-colour LBM model was adopted by Gac and Gradoń [30] to simulate droplet impingement on spherical particles. They found that with the increase of Weber number, the droplet could go from merging with the particle to being ripped and Skirt scattering. Yan [31] proposed a scheme of Lattice Boltzmann model and validated by the simulation of droplet wetting on heterogeneous surfaces. They further proved the capability of LBM as a tool for solving wetting related cases. Shen et al. [32] applied the famous Shan-Chen LBM model to study the droplet impact on a spherical obstacle. Different deformation processes were observed: moving, spreading, nucleating, and falling, and whether the droplet will splash or not depends on the impact velocity and the surface wettability. A. Merdasi and M. Bakhshan et al. [33,34] studied the droplet impingement on rectangular obstacles in a channel. The He-Chen-Zhang method and multi-relaxation-time (MRT) collision operator are adopted respectively in their studies. The outcomes show that a higher gravity, a larger Weber number, an increased obstacle hydrophobicity as well as a lower viscosity would contribute to the droplet's breaking up.

In this paper, the multi-component multiphase pseudopotential LBM model is adopted to study the impingement of a droplet on the vertex of a conical obstacle. A modified method for boundary treatment is introduced to correctly represent the droplet's wetting on the hypotenuses. The model is first validated through Laplace law, D^2 law and equilibrium wetting test, and factors like gravity magnitude, surface wettability and surface temperature are studied for their influence on the droplet's impingement. This study aims to reveal the characteristics of the impingement between a droplet and a conical obstacle and provide fundamental support to related engineering applications such as spray cooling.

Numerical methodology

In this section, the multi-component multiphase lattice Boltzmann method adopted in this study, which is based on the Gong-Cheng model [35] and Shan-Chen model [36], will be discussed. The model contains 2 components: water and non-condensable gas, with the phase of the water component changing between liquid and vapour. The Bhatnagar–Gross–Krook (BGK) collision operator is adopted as its simpler form can provide a more flexible boundary condition treatment.

The pseudopotential multi-component multiphase lattice Boltzmann model

The Lattice Boltzmann Equation (LBE) for momentum is listed below, which contains collision and streaming steps [37]:

$$f_{\sigma,i}(x+e_i\delta t, t+\delta t) - f_{\sigma,i}(x,t) = -\frac{1}{\tau_\sigma}(f_{\sigma,i}(x,t) - f^{eq}_{\sigma,i}(x,t)) \tag{2.1.1}$$

where τ_σ is the dimensionless collision relation time of the σ_{th} component, and it's determined by the kinetic viscosity of the fluid.

$$\nu_\sigma = \frac{1}{3}c^2(\tau_{\sigma,f} - \frac{1}{2})\delta t \tag{2.1.2}$$

In this system, there are two different components, respectively water (either in the vapour phase or liquid phase) and non-condensable gas. e_i is the lattice velocity vector and i stands for the lattice velocity direction. For the D2Q9 model there are 9 directions, so i ranges from 0 to 8. The discrete velocity for each direction is:

$$e_i = \begin{cases} (0,0) & i = 0 \\ c\left(\cos\frac{(i-1)\pi}{2}, \sin\frac{(i-1)\pi}{2}\right) & i = 1,\ldots,4 \\ \sqrt{2}\,c\left(\cos\frac{(2i-9)\pi}{4}, \sin\frac{(2i-9)\pi}{4}\right) & i = 5,\ldots,8 \end{cases} \tag{2.1.3}$$

where c is the reference lattice velocity.

$f_{\sigma,i}(x,t)$ and $f^{eq}_{\sigma,i}(x,t)$ are the distribution function and equilibrium distribution function of the σ_{th} component with the velocity e_i at lattice x and time$t$, respectively.

Corresponding to the D2Q9 model, the momentum equilibrium distribution function is incorporated as [38]:

$$f^{\text{eq}}_{\sigma,i} = \omega_i\rho_\sigma\left[1 + 3\frac{e_i\cdot u_\sigma}{c^2} + \frac{9}{2}\frac{(e_i\cdot u_\sigma)^2}{c^4} - \frac{3}{2}\frac{(u_\sigma)^2}{c^2}\right] \tag{2.1.4}$$

where ω_i is the weight coefficients, equalling to $4/9$ for$i = 0$, $1/9$ for$i = 1 \sim 4$, and $1/36$ for$i = 5 \sim 8$.

The density and velocity of each component can be calculated as:

$$\rho_\sigma(x,t) = \sum_i f_{\sigma,i}(x,t) \tag{2.1.5}$$

$$u_\sigma(x,t) = \frac{\sum_\sigma 1/\tau_\sigma \sum_i e_i f_{\sigma,i}(x,t)}{\sum_\sigma 1/\tau_\sigma \sum_i f_{\sigma,i}(x,t)} + \frac{F_\sigma(x,t)}{\sum_\sigma 1/\tau_\sigma \sum_i f_{\sigma,i}(x,t)} \tag{2.1.6}$$

where $F_\sigma(x,t)$ is the sum of forces applying to the σ_{th} component at the location x and at time$t$. The real velocity can be acquired by averaging the velocity before and afterδt, incorporated as [39]:

$$U_\sigma(x,t) = \frac{\sum_i e_i f_{\sigma,i}(x,t)}{\rho_\sigma(x,t)} + \frac{\delta t F_\sigma(x,t)}{2\rho_\sigma(x,t)} \tag{2.1.7}$$

And the total density and velocity are written as [40]:

$$\rho(x,t) = \sum_\sigma \rho_\sigma(x,t) \tag{2.1.8}$$

$$U(x,t) = \frac{1}{\rho(x,t)}\sum_\sigma \rho_\sigma(x,t)U_\sigma(x,t) \tag{2.1.9}$$

In this simulation, four different forces are considered to apply on a fluid node: the attractive force between the same components, the repulsive force between different components, the interaction force between the solid substrate and fluid components, and the gravity force. The thermophoretic force was also considered but its magnitude is too minimal compared to other forces hence neglected in this case. The interaction forces between fluid components are calculated according to Gong and Cheng's method [35]:

$$F_{\sigma,\sigma} = -\beta\psi_\sigma(x)\sum_{x'} G_\sigma(x,x')\psi_\sigma(x') + \frac{(1-\beta)}{2}\sum_{x'} G_\sigma(x,x')\psi^2_\sigma(x') \tag{2.1.10}$$

$$F_{\sigma,\sigma'} = -\varphi_\sigma(x)\sum_{x'} G_{\sigma'}(x,x')\varphi_{\sigma'}(x') \tag{2.1.11}$$

where σ' stands for the other component and x' stands for the neighbouring lattice. β is the tuneable weighting factor. And the solid–fluid interaction force is shown below:

$$F_{\sigma,s} = -(\psi_\sigma(x))^2\sum_{x'} G_s(x,x')s(x') \tag{2.1.12}$$

for $s(x')$ the value varies from 0 to 1, depending on whether the lattice on x' is fluid phase or solid. In Eq., and, the value of $G_{x,x',s}(x,x')$ is determined by the distance between the fluid nodes. The relationship between them is listed below [41]:

$$G_{\sigma,\sigma',s}(x') = \begin{cases} 2g_{\sigma,\sigma's} & |x'-x| = 1 \\ g_{\sigma,\sigma's}/2 & |x'-x| = \sqrt{2} \\ 0 & otherwise \end{cases} \tag{2.1.13}$$

$\psi_\sigma(x)$ represents the effective mass of the σ_{th} component at node$x$. In the Shan-Chen model, the effective mass is given as [42]:

$$\psi_\sigma(x) = \sqrt{\frac{2(p_\sigma - c_s^2\rho_\sigma)}{c_0 g_\sigma}} \tag{2.1.14}$$

By comparing Eq. with Eq., it can be found that the force coefficient g_σ is cancelled out. Different from pseudo-potential $\psi_\sigma(x)$, $\varphi_\sigma(x)$ is chosen as $\varphi_\sigma(x) = \rho_\sigma(x)$ to enforce a proper component distribution.

Zhang et al. [43] compared different methods to calculate the gravity force. In this paper, to ensure the conservation of the average mass velocity, the gravity force is given as:

$$F_{\sigma,g} = (\rho_\sigma - \rho_{avg})g \tag{2.1.15}$$

where ρ_{avg} is the average density of the computational domain.

The lattice Boltzmann model for thermal filed with phase change term

The energy lattice Boltzmann equation used in this paper is given as [44]:

$$g_{\sigma,i}(x+e_i\delta t, t+\delta t) - g_{\sigma,i}(x,t) = -\frac{1}{\tau_{\sigma,\text{T}}}(g_{\sigma,i}(x,t) - g^{\text{eq}}_{\sigma,i}(x,t)) + \delta t\omega_i\phi_\sigma \tag{2.2.1}$$

In Eq., $\tau_{\sigma,\text{T}}$ is the temperature relaxation time, which is related to the thermal diffusivity:

$$\alpha_\sigma = \frac{1}{3}c^2(\tau_{\sigma,\text{T}} - \frac{1}{2})\delta t \tag{2.2.2}$$

$g^{eq}_{\sigma,i}(x,t)$ is the corresponding thermal equilibrium distribution function that can be obtained as:

$$g_{\sigma,i}^{eq}(x,t) = \omega_i \mathrm{T}\left[1 + 3\frac{e_i \cdot U}{c^2} + \frac{9}{2}\frac{(e_i \cdot U)^2}{c^4} - \frac{3}{2}\frac{(U)^2}{c^2}\right] \tag{2.2.3}$$

The phase change source term ϕ_σ is given below, as obtained by C. Zhang et al. [45]:

$$\phi_\sigma = T_\sigma\left[1 - \frac{1}{\rho_\sigma c_{v,\sigma}}\left(\frac{\partial p_\sigma}{\partial T_\sigma}\right)_{\rho_\sigma}\right]\nabla \cdot U_\sigma + \left[\frac{1}{\rho_\sigma c_{p,\sigma}}\nabla(\lambda_\sigma \nabla T_\sigma) - \nabla \cdot \left(\frac{\lambda_\sigma}{\rho_\sigma c_{p,\sigma}}\nabla T_\sigma\right)\right] \tag{2.2.4}$$

where λ is the thermal conductivity, c_v and c_p are the thermal specific heat at constant volume and pressure respectively. In this simulation, for the non-condensable gas component, the thermal specific heat is set to be 1, so the first term in Eq. will be 0. For the macroscale temperature, the temperature for each component can be obtained as below:

$$\mathrm{T}_\sigma(x,t) = \sum_i g_{\sigma,i}(x,t) \tag{2.2.5}$$

and the temperature for the mixture is

$$\mathrm{T}(x,t) = \frac{1}{\rho(x,t)c_v}\sum_\sigma \rho_\sigma(x,t)c_{\sigma,v}\mathrm{T}_\sigma(x,t) \tag{2.2.6}$$

The equation of state

The Peng-Robinson equation of state (P-R EOS) is adopted in this simulation to couple the momentum with the thermal LB model. The equation is given as

$$p = \frac{\rho RT}{1-b\rho} - \frac{a\rho^2\varepsilon(T)}{1+2b\rho-b^2\rho^2} \tag{2.3.1}$$

where $a = \frac{0.457235R^2T_c^2}{p_c}$, $b = \frac{0.077796RT_c}{p_c}$ and $\varepsilon(T) = \left[1 + (0.37464 + 1.54226\omega - 0.26992\omega^2)\left(1 - \sqrt{T/T_c}\right)\right]$, where the subscript c denotes critical state. ω is the acentric factor and is set to $\omega = 0.344$, and a, b, R are set to 3/49, 2/21 and 1 respectively [35]. In this case, β in Eq. equals to 1.16 for the water component. To improve the numerical stability at larger density ratios, Hu et al. [46] introduced a coefficient k to modify the EOS, so the model can remain its stability when simulating cases with larger density ratios. The EOS after the modification is written as

$$p = k\left(\frac{\rho RT}{1-b\rho} - \frac{a\rho^2\varepsilon(T)}{1+2b\rho-b^2\rho^2}\right) \tag{2.3.2}$$

where $0 < k < 1$.

For the non-condensable gas component, the ideal gas equation is used, as listed below:

$$p = \rho RT \tag{2.3.3}$$

Correspondingly, the β in Eq. equals 1.

Geometry setup and boundary conditions

The simulations in this study are performed in a 2D rectangular domain in order to save computation resource, with the dimension of$L_x \times L_y$. The conical obstacle is placed in the centre of the bottom substrate, with the angle of its vertex being90°. The left and right boundaries of the computational domain are set as periodic boundaries, while non-slip bounce-back boundaries [47] are adopted for the top and bottom boundaries, as well as the upper surface of the obstacle. The halfway bounce-back scheme proposed by Zou et al. [48] is used at the non-slip boundaries. For the left and right boundaries, the boundary equations go as $f_{\sigma,i}((0-1,y),t) = f_{\sigma,i}((L_x,y),t)$ for the left boundary and $f_{\sigma,i}((L_x+1,y),t) = f_{\sigma,i}((0,y),t)$ for the right boundary. For thermal boundary conditions, $g_{\sigma,i}((0-1,y),t) = g_{\sigma,i}((L_x,y),t)$ and $g_{\sigma,i}((L_x+1,y),t) = g_{\sigma,i}((0,y),t)$ can be obtained.

The non-slip bounce-back boundary conditions applied to the substrates can be written in the following forms. Taking the bottom substrate as an example: $f_{\sigma,2}(x,\ t) = f_{\sigma,4}(x,\ t)$, $f_{\sigma,5}(x,t) = f_{\sigma,7}(x,t) + 0.5(f_{\sigma,3}(x,t) - f_{\sigma,1}(x,t)) - 0.25(F_{\sigma,x} + F_{\sigma,y})$ and $f_{\sigma,6}(x,\ t) = f_{\sigma,8}(x,\ t) + 0.5(f_{\sigma,1}(x,t) - f_{\sigma,3}(x,t)) + 0.25(F_{\sigma,x} - F_{\sigma,y})$. For the hypotenuses of the obstacle, due to its inclined angle, the boundary condition is achieved by coupling the tuned non-slip bounce-back scheme with Filippova and Hänel's scheme [49].

As shown in Fig. 2.2, the relative distance between the fluid node that is closest to the solid node and its closest neighbouring physical boundary is represented by a variable$q$, given as

$$q = \frac{|r_f - r_w|}{|r_f - r_b|},\ 0 < q < 1 \tag{2.4.1}$$

where r_w represents the location of the actual physical boundary.

To calculate the boundary momentum distribution function, a virtual equilibrium distribution function is constructed, written as:

$$f_i(r_b,t) = w_i\rho(r_f,t)\left[1 + \frac{3}{c^2}e_i \cdot u_{bf} + \frac{9}{2c^4}(e_a \cdot u_f)^2 - \frac{3}{2c^4}u_f \cdot u_f\right] \tag{2.4.2}$$

where u_{bf} is a virtual velocity to de determined.

The momentum distribution function after colliding with the boundary can be obtained as:

$$f_i(r_b,t) = (1-\chi)f_i(r_f,t) + \chi f_i(r_b,t) + 2\omega_i\rho\frac{3}{c^2}e_i \cdot u_w \tag{2.4.3}$$

where u_w is the velocity of the wall, and it equals 0 in this case.

In Eq. (2.4.2) and (2.4.3), the values of u_{bf} and χ are related to the value of$q$:

$$\begin{cases} u_{bf} = u_f(r_f + e_i\delta t, t),\ \chi = \dfrac{2q-1}{\tau - 2} & q < 1/2 \\ u_{bf} = \dfrac{q-1}{q}u_f + \dfrac{1}{q}u_w,\ \chi = \dfrac{2q-1}{\tau} & q \geqslant 1/2 \end{cases} \tag{2.4.4}$$

It can be observed that in this case, $f_i(r_b,t)$ matches the standard bounce-back scheme when$q = 1/2$. However, the standard bounce-back boundary condition suffers from problems such as low numerical accuracy, and the lack of anti-slip terms causes the droplet unable to achieve a stable wetting condition. Hence, the modified non-slip bounce-back scheme is applied here as an alternative. Taking the left-side hypotenuse as an example, the modified non-slip bounce-back boundary condition can be written as:$f_6(x,\ t) = f_8(x,\ t)$, $f_2(x,t) = f_4(x,t) + 0.5(f_7(x,t) - f_5(x,t)) + F_x/\kappa_x + F_y/\kappa_y$ and $f_3(x,\ t) = f_1(x,\ t) + 0.5(f_5(x,t) - f_7(x,t)) + F_x/\kappa_x + F_y/\kappa_y$, where κ_x and κ_y are adjustable parameters related to the angle of the hypotenuse and the solid–fluid interaction force coefficientG_s. While for fluid nodes with other values of$q$, the algorithm - is adopted. By introducing the modified boundary condition treatment method, a steady wetting condition for droplets on hypotenuses can be achieved.

For the thermal boundary condition, constant temperatures are applied to the lower solid substrates. The lower substrates are set at 5 different temperatures throughout this study as $T_b = T_s + dT$, with dT being 0, $0.05T_c$, $0.1T_c$, $0.2T_c$ and $0.3T_c$ respectively. The upper substrate adopts the thermal non-equilibrium extrapolation scheme in all cases.

Results and discussion

Model validation

In this section, the model will be validated through 3 different simulations: the Laplace law, the D^2 law, and its capability to achieve a stable wetting condition on an inclined surface.

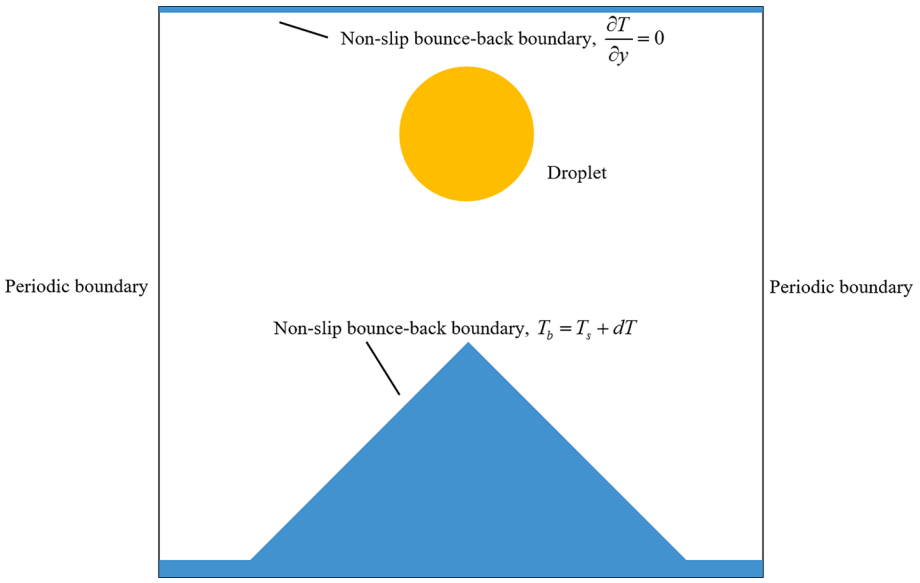

Fig. 2.1. Schematic of the computational domain.

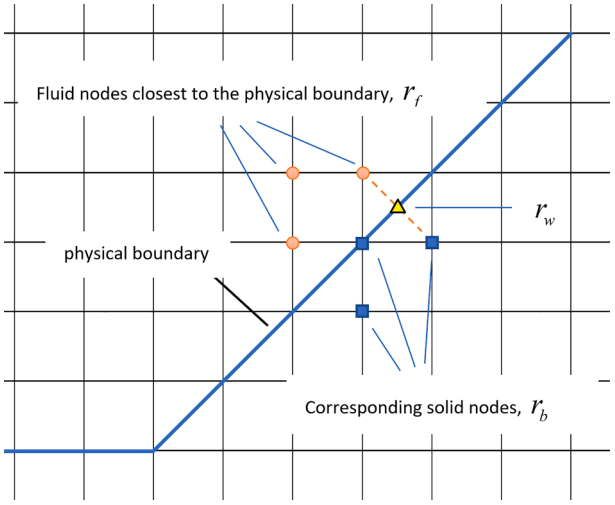

Fig. 2.2. Illustration of the hypotenuse boundary treatment using Filippova and Hänel's scheme.

The Laplace law

The Model is compared to the Laplace law for verification. The Laplace law reflects the relationship between the pressure difference across the vapour/droplet interface Δp and the droplet radius$R$, that the pressure difference is inversely proportional to the droplet radius with the proportionality coefficient equal to the surface tensionσ. The simulation is conducted in the above-mentioned geometry setup but without the conical obstacle. The droplet is placed in the centre of the domain, of which the density is initialized as

$$\rho_\sigma(x,y) = \frac{\rho_{\sigma,\text{in}} + \rho_{\sigma,\text{out}}}{2} - \frac{\rho_{\sigma,\text{in}} - \rho_{\sigma,\text{out}}}{2}\tanh\left[\frac{2(\sqrt{(x-x_0)^2+(y-y_0)^2} - R_0)}{W}\right] \quad (3.1.1)$$

where $\rho_{\sigma,\text{in}}$ and $\rho_{\sigma,\text{out}}$ are the density of the σ_{th} component inside and outside of the dropwise, R_0 is the radius of the droplet and W is the thickness of the initial interface width. The simulation is carried out at the temperature of$T = 0.8T_c$, $T = 0.85T_c$ and$T = 0.9T_c$, with the saturated liquid and vapour density listed in Table 1.

Table 1
Saturated density distribution at different temperatures.

	$0.8T_c$	$0.85T_c$	$0.9T_c$
ρ_{liquid}	7.2039	6.6293	5.9079
ρ_{vapor}	0.1971	0.3413	0.5801

The initial density of the non-condensable gas is set at 0.0017, so a weight fraction of around 0.025 % can be achieved. The droplet radius ranges from 20 lattice units (l.u.) to 50 l.u. at an interval of 10 l.u. and the relationship between radius and pressure difference is displayed in Fig. 3.1. It can be found that the model satisfies the Laplace law.

The D^2 law

The D^2 law tells that the square of the droplet diameter should be linear to time throughout the evaporating process, given the thermal-physics parameters are kept constant [50]. A simulation is carried out to check the model's capacity to simulate cases with phase change. The simulation setup is similar to that in section 3.1.1, except that the temperature of the surrounding vapour is set at a higher value

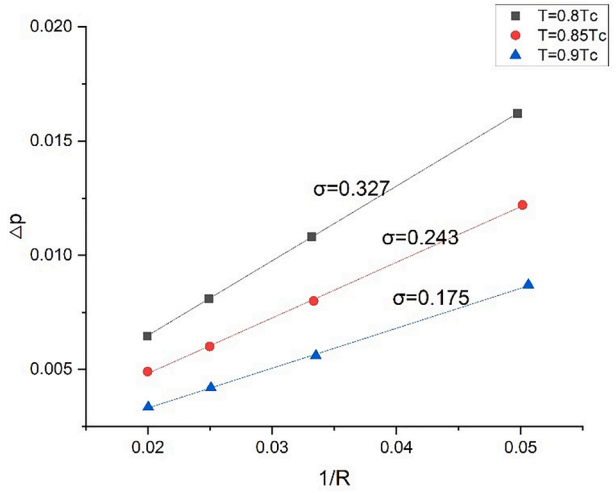

Fig. 3.1. The relationship of pressure drop between the liquid and gas components and droplet radius for $T = 0.8T_c$, $T = 0.85T_c$ and $T = 0.9T_c$.

$T_{vap} = T_{liq} + \Delta T$ than the liquid droplet. Also, a non-equilibrium extrapolation momentum boundary condition is applied to all boundaries, to allow the vapour to escape from the simulating domain so the density and the pressure of vapour can remain constant. Other thermal-physics parameters, such as thermal diffusivity and specific heat capacity, are kept constant. A droplet with an initial radius of 40 l.u. is placed in the centre of the domain, and after the first 10^6 timesteps, the relation between R^2/R_0^2 and timesteps is shown in Fig. 3.2.

It can be observed that the evaporating curve obeys the D^2 law, meaning that the model is capable of simulating phase change cases.

Wettability on inclined surfaces

As we adopted a modified boundary treatment method in this study for simulating the droplet wetting on inclined surfaces, the corresponding simulations are carried out to prove that the droplet can achieve a stable contact angle. The droplet with a radius of 30 l.u. is placed in the centre on a hypotenuse inclined at 45°, which is the same as the geometry setup in this study. The upper and lower boundaries are using the half-way bounce-back boundary conditions, while the left and right boundaries are periodic boundaries. The modified boundary condition treatment method introduced in section 2.4 is adopted for the inclined surface. There are no external forces applied to the domain, and the temperature is set constant. Surrounding the droplet is vapour and non-condensable gas. The different contact angles of the droplet can be achieved by tuning the interaction force coefficient G_s in the formula as well as κ_x andκ_y. The relationship of G_s and the equilibrium contact angle are shown in Fig. 3.3, proving that stable wetting conditions can be achieved using this method.

Droplet impingement on the vertex of a conical obstacle

The way that a droplet behaves upon impinging against a vertex depends on many factors, like the property of the droplet and the angle of the impingement. Cases like off-centre impingement and impacting with an angle even increases the possibility of different outcomes. As we cannot investigate each of them in this paper, we selected the most representative case, which is a symmetric impact on a cone with a fixed vertex angle at 90° The geometry setup is as that shown in Fig. 2.1, and the initial temperature of the system is set at the saturated temperature$T_s = 0.85T_c$. A droplet with a radius of 30 l.u. is initially set at the height of 225 l.u. and stabilized for 5000 timesteps before gravity force is applied, for the system to reach a thermodynamic equilibrium state. The effect of different factors, like the magnitude of gravity, the surface wettability of the obstacle, and the temperature of the obstacle are studied. Due to the limitation of the 2D model, the effect of surface tension on horizontal direction is not considered in this simulation.

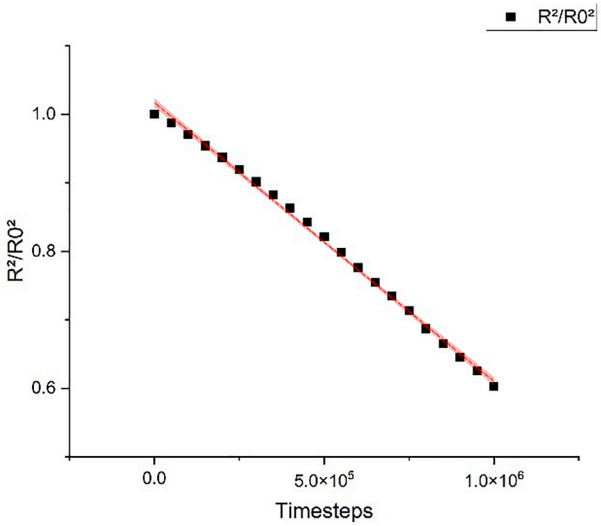

Fig. 3.2. Normalized square of droplet diameter versus the evaporating time.

The effect of gravity

When studying the droplet impingement scenarios, two different approaches are usually considered. The first one is to ignore the gravity force while giving the droplet an initial velocity. The second one is not giving the droplet initial velocities while letting the droplet free fall, driven by the effect of gravity. Since in this paper, both upper and lower boundaries are bounce-back boundaries, the first approach cannot reach the ideal effect as the drag force will stop the droplet from accelerating. Thus, the second approach is adopted in this paper.

According to the research of Rahmati et al. [51], the parameters associated with the impingement, like the impingement velocity, Reynold number, Weber number and Bond number can be given in the following forms:

$$v_0 = \sqrt{2g(H' - r)} \tag{3.2.1}$$

$$Re = \frac{v_0 d}{\upsilon} \tag{3.2.2}$$

$$We = \frac{\rho_l v_0^2 d}{\sigma} \tag{3.2.3}$$

$$Bo = \frac{\rho_l d^2 g}{\sigma} \tag{3.2.4}$$

where H' is the initial height of the droplet centre, d is the droplet diameter, υ is the kinematic viscosity of the droplet. Also, the dimensionless time is given as

$$t^* = \frac{t}{\sqrt{d/g}} \tag{3.2.5}$$

Note that in this study, the dimensionless time counts from the moment that gravity is applied.

In this simulation, three different magnitudes of gravity are considered, respectively 1×10^{-5}, 2×10^{-5} and 3×10^{-5}. As the initial height is fixed at 225 l.u. as well as the initial fluid properties, the corresponding dimensionless parameters are given in Table 2.

For each gravity magnitude, three different stages of the impingement process are investigated: the first stage is when the droplet fully wraps the vertex, and the second stage is the moment before the droplet breaks apart and disconnects at the vertex. The third stage is when the droplet slides down against the hypotenuse with its advancing and receding contact angles reaching a relatively equilibrium state. The substrates are of neutral wettability and no heating condition is applied. As shown in Fig. 3.4, for$g = 1 \times 10^{-5}$, the droplet rebounds after impinging against the vertex and eventually stops while wrapping the vertex with the contact angle on each side equal to approximately 84°. That's because, for a small gravity force, the momentum of the droplet is too weak to overcome the interaction force between the liquid molecules wrapping the vertex. While for $g = 2 \times 10^{-5}$ and $g = 3 \times 10^{-5}$, the gravity force and momentum can overcome the interaction force at the vertex and allow the droplet to rupture. Besides the fact that under a stronger gravity force the droplet gains a larger vertical velocity, the droplet also appears to be flatter while sliding down along the hypotenuse. The advancing and receding contact angles in stage 3 are 91.4° and 78.1° for$g = 2 \times 10^{-5}$, while those for $g = 3 \times 10^{-5}$ are 96.5° and 69.3°.

The effect of surface wettability

As the droplet impinges and slides down the hypotenuse, the surface wettability would have a significant effect on the behaviour of the droplet. However, it's very difficult to change the surface wettability in real life without changing other parameters of the surface, like the

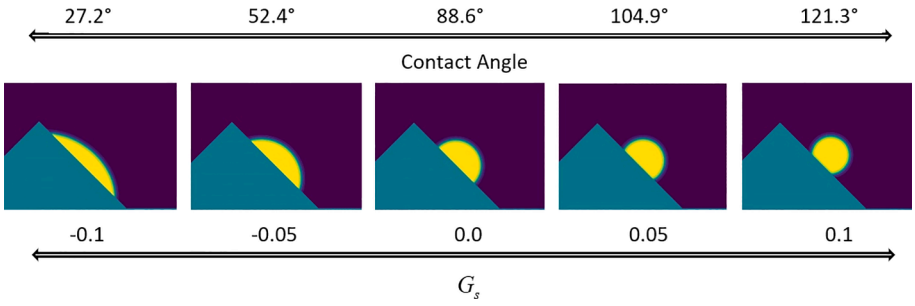

Fig. 3.3. Different wetting conditions of the droplet on an inclined surface.

Table 2
Corresponding parameters of different gravity magnitudes.

g	v_0	Re	We	Bo
0.00001	0.05	18.00	4.09	0.98
0.00002	0.07	25.46	8.18	1.96
0.00003	0.09	31.18	12.28	2.95

geometry, while the simulation approach doesn't meet such limitations. Ma et al. [52] used the LBM method to study the droplet impingement on an inclined surface with different wettability, but the ZSC model applied in the study needs improvement in terms of thermodynamic consistency. In this study, we applied 4 different wetting conditions by changing the value of G_s in Eq. (2.1.12). The gravity is set at $g = 2 \times 10^{-5}$, and no heating condition is added. The results are shown in the snapshot below. As the geometry setup is symmetric, here only the right half of the obstacle is shown.

In Fig. 3.5, (a)-(d) refer to the value of$G_s = -0.05$, 0, 0.05 and 0.1,

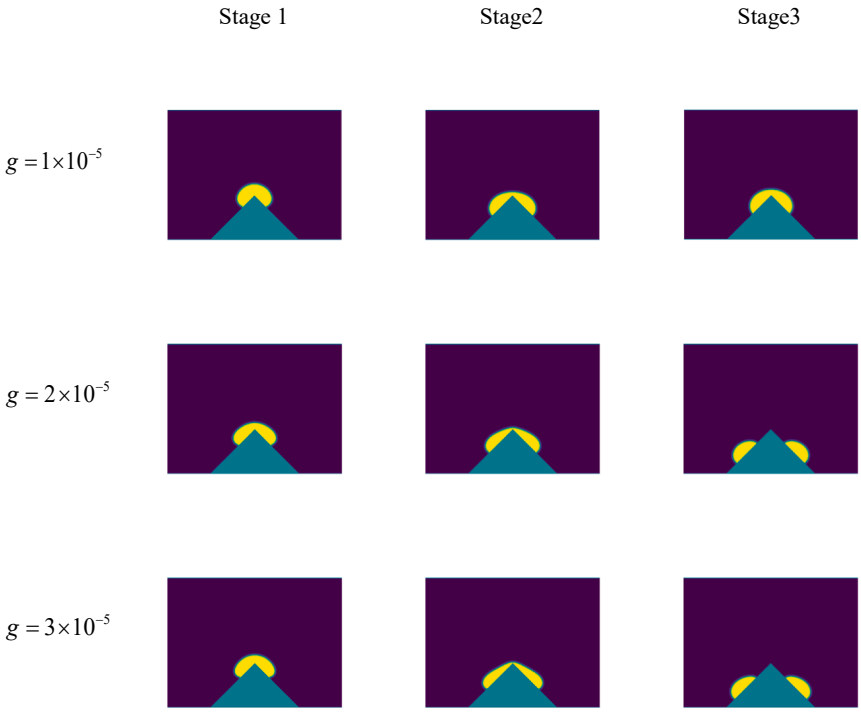

Fig. 3.4. Droplet impingement on the cone vertex under different gravity magnitudes.

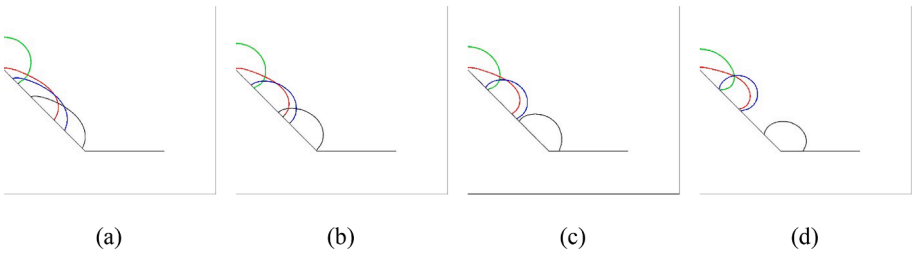

Fig. 3.5. Snapshot of the droplet impinging on surfaces of different wettability.

with the corresponding contact angle of the droplet on a flat surface being 69.9°, 88.5°, 104.5° and120.4°. These 4 snapshots with outlines of different colours are taken at: $t^* = 2.31$ for green, $t^* = 3.46$ for red, $t^* = 4.91$ for blue and $t^* = 8.08$ for black. At$t^* = 2.31$, it can be found that the difference between advancing contact angle is quite minor, as the interaction between the droplet and the surface just started. As time proceeds to$t^* = 3.46$, the effect of surface wettability becomes obvious, and the advancing contact angle gradually reaches a stable value. While on the vertex of the obstacle, the droplet starts to rupture. For$t^* = 4.91$, the droplet fully breaks apart and as the interaction force with the other part disappears, the force acting on the receding contact line becomes the interaction force between the liquid and the surface, which is much smaller than the interaction force between liquid molecules on a hydrophobic surface. That results in the receding contact line moving quickly downwards, so does the centre of gravity of the droplet. A phenomenon similar to weightlessness appears, and the height of the droplet's advancing contact line merely moves on hydrophobic surfaces. On hydrophilic surfaces however, there is no such phenomenon observed, as the interaction force between the liquid molecules is weaker than that between liquid and surface. In the last snapshot, the droplet slides down the surface with both advancing and receding angles relatively stable. From the figure, it can be found that the velocity of the droplet on a hydrophilic surface is more linear, but on a hydrophobic surface due to the weightlessness phenomenon the velocity profile goes through a stall when the droplet rupture on the vertex. And the droplet on hydrophobic surface has a larger overall velocity than on a hydrophilic surface, due to a smaller interaction force with the surface. This is further proved in Fig. 3.6, in which the relationship between the droplet centre point and dimensionless time is shown.

The effect of surface temperature

Despite that the impingement of droplets has been studied by a lot of researchers, the effect of temperature is seldomly considered. One of the reasons is that the process of impingement happens in a very short time, hence the evaporation of droplets can be ignored. However, we have noticed that the temperature of the obstacle surface has a significant influence on the behaviour of the droplet, especially when the temperature is high enough when the famous Leidenfrost effect can be observed. Hence in this section, the surface of the conical obstacle is set at different temperatures, and the behaviour of the droplet is studied.

In Fig. 3.7 the snapshots of the droplets impinging on surfaces of different temperatures are presented. All other parameters are kept the same, with gravity force being $g = 2 \times 10^{-5}$ and surface wettability being neutral ($G_s = 0$). The temperature of the surface is written as$T_b = T_s + dT$, as introduced in section 2.4, with $dT = 0.05$ in Fig. 3.7 (a), $dT = 0.1$ and 0.2 in (b) and (c), $dT = 0.3$ in (d) correspondingly. Jakob number which can be written as

$$Ja = \frac{(T_w - T_s)c_p}{h_{lv}} \tag{3.2.6}$$

is used to measure the influence of the substrate temperature, where h_{lv} is the liquid–vapour latent heat. For picture (a)-(d), the Jakob number are 0.04, 0.075, 0.15 and 0.23 respectively. The time intervals are kept the same as in section 3.2.2, and the dropwise at different moments are marked in the same colours as above. It can be found that in Fig. 3.5 (a) and (b), the dropwise is similar to that in Fig. 3.5(c) and (d), as a higher temperature reduces the density of droplets around the contact line thus reducing interaction force between the liquid and solid substrate. If the temperature keeps increasing, as shown in picture (c), the droplet detaches from the solid surface, which can be explained by the Leidenfrost phenomenon: the evaporation process is so fast that a vapor layer appears between the droplet and the hot surface, making the droplet float above the surface [53]. The existence of the vapour layer removes all the interaction force between the droplet and the surface, making the droplet slide down at the maximum rate possible. From picture (c) and (d) one can find that there is no major difference between those two cases, the reason is the vapour layer works as a heat insulation cushion in the Leidenfrost phenomenon, and vapour has a much lower heat conductivity than water. As a result, the increase in surface temperature doesn't affect the impingement process significantly. Also, there is merely any influence on the droplet velocity as the droplet is already levitating.

Fig. 3.8 shows the temperature counter of the flow field at for ranging from 0.04 to 0.23. Apart from the difference in the shape of the dropwise, one can also notice that in Fig (a) and (b), the temperature at the junction line between the droplet and the solid surface is nearly the same as the substrate temperature, while it gradually decreases with the increase of the distance from the obstacle surface. In Fig (c) and (d), the temperature in the dropwise is almost constant as the droplet is in the Leidenfrost stage, the vapour layer prevents the heat of the substrate from directly entering the droplet. Moreover, the velocity of the droplet is rapid enough for preventing the droplet from absorbing too much heat in the process, so apart from the vaporized part, the liquid remains relatively cool compared to the surrounding vapour.

Fig. 3.9 presents the relationship between the droplet's mean temperature and dimensionless time. For different values that aren't 0, the droplet is heated in the impingement process at different rates. Overall, the mean temperature when tops all the scenarios, followed by and, and has the lowest mean temperature. It's noticeable that the droplet has a lower temperature in the Leidenfrost stage even though the number is much higher, which proves that the vapour layer is blocking heat from entering the droplet. Also, the deformation of the droplet causes minor temperature fluctuations, as can be seen from the curve for, the reason behind this is the viscous dissipation caused by the deformation during the process of impacting. The mean temperatures of and raises at a

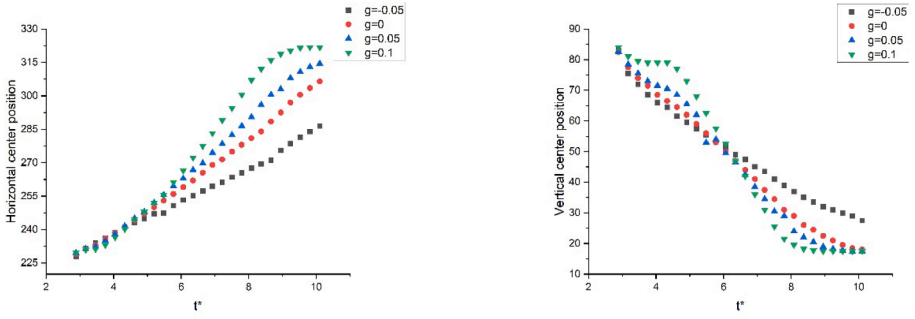

Fig. 3.6. Relationship between the droplet position and dimensionless time.

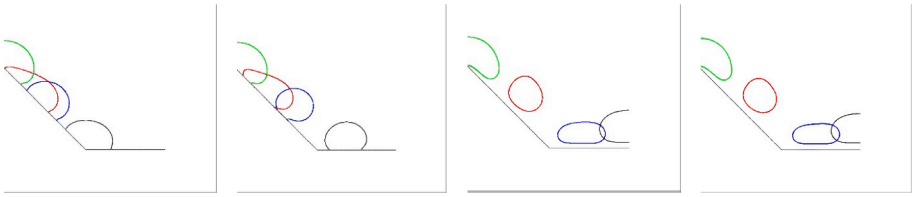

Fig. 3.7. Snapshot of the droplet impinging on surfaces of different temperatures.

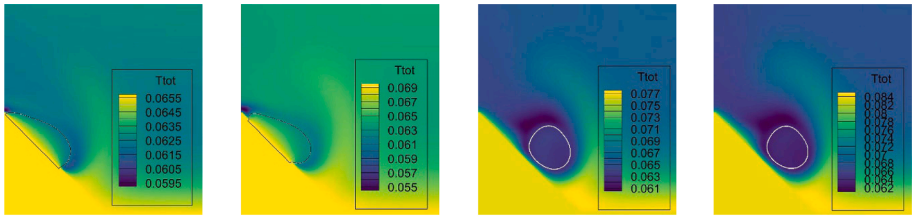

Fig. 3.8. Temperature profiles of the flow field at $t^* = 3.46$ for different surface temperatures.

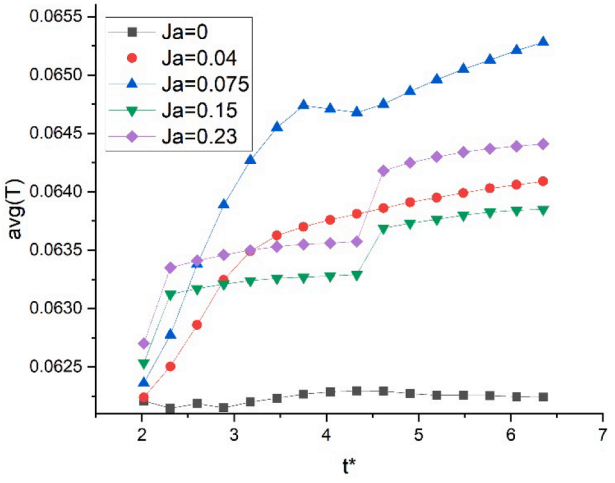

Fig. 3.9. Mean temperature of the droplet during the impingement process.

higher rate when, and when moves closer to 4 the rate slows down gradually. This can be explained by the droplet morphologic figures in Fig. 3.7, where one can see that the contact line between the droplet and the surface has decreased sharply when approaches 4.91, and a reduced heat exchange size results in the reduced temperature rising rate. For and, a sharp increase in the droplet temperature can be observed between and, and according to Fig. 3.7, the droplet is impinging on the vertex of the obstacle and bottom substrate respectively during that time. The effect of impact could bring a reduced vapour layer thickness, if not a temporary connection between the droplet and the superheated substrate. After that, both droplets get heated up at lower rates.

Conclusion and prospection

In this paper, a multi-component multiphase Lattice Boltzmann model is developed to study the process of a droplet impinging on the vertex of a conical obstacle. The model is modified with a mixed non-slip bounce-back boundary treatment method and validated being able to simulate the droplet's wetting on hypotenuses. The effect of different factors, such as gravity magnitude, surface wettability and substrate temperature, is studied. The present investigation fucuses on the morphology of the droplet, its velocity profile and temperature distributions. The following can be concluded:

1. Three different behaviours of droplet are observed in the impingement process, namely: wrapping the vertex, sliding down against the hypotenuse, and sliding down levitated. Wrapping the vertex is more likely to happen when gravity is low, and the surface is hydrophobic, while a more hydrophilic surface increases the chance of the droplet sliding down against the hypotenuse. A higher temperature and a more hydrophobic surface make the droplet more likely to detach from the surface and slide down levitated.
2. An increased surface hydrophobicity in general increases the sliding velocity of the droplet, however on hydrophobic surfaces, the non-equilibrium wetting condition on the receding edge at the moment of rupturing would cause a temporary weightlessness phenomenon that stops the droplet from sliding down.
3. Leidenfrost effect happens in cases where $Ja \geqslant 0.15$. The heat transfer rate is then reduced as the vapour layer between the droplet and substrate has a lower heat conductivity. The highest droplet mean temperature is observed when $Ja = 0.075$. On the other hand, the droplet in the Leidenfrost stage has a higher velocity as the interaction force between the droplet and surface disappears.

Declaration of Competing Interest

The authors declare that they have no known competing financial interests or personal relationships that could have appeared to influence the work reported in this paper.

Data availability

No data was used for the research described in the article.

Acknowledgements

This paper is financially supported by project ThermaSMART (H2020-MSCA-RISE-778104-ThermaSMART), and scholarship from the China Scholarship Council (CSC).

References

[1] H.-J. Chang, M.H. Tsai, W.-S. Hwang, The simulation of micro droplet behavior of molten lead-free solder in inkjet printing process and its experimental validation, App. Math. Model. 36 (7) (2012) 3067–3079.

[2] J. Léopoldès, A. Dupuis, D.G. Bucknall, J.M. Yeomans, Jetting micron-scale droplets onto chemically heterogeneous surfaces, Langmuir 19 (23) (2003) 9818–9822.

[3] J.D. Benther, J.D. Pelaez-Restrepo, C. Stanley, G. Rosengarten, Heat transfer during multiple droplet impingement and spray cooling: review and prospects for enhanced surfaces, Int. J. Heat Mass Transf. 178 (2021), 121587.

[4] I.V. Roisman, J. Breitenbach, C. Tropea, Thermal atomisation of a liquid drop after impact onto a hot substrate, J. Fluid Mech. 842 (2018) 87–101.

[5] M. Rein, Phenomena of liquid drop impact on solid and liquid surfaces, Fluid Dyn. Res. 12 (2) (1993) 61–93.

[6] J.S. Eow, M. Ghadiri, Electrostatic enhancement of coalescence of water droplets in oil: a review of the technology, Chem. Eng. J. 85 (2) (2002) 357–368.

[7] Y. Cheng, F. Wang, J. Xu, D. Liu, Y. Sui, Numerical investigation of droplet spreading and heat transfer on hot substrates, Int. J. Heat Mass Transf. 121 (2018) 402–411.

[8] S. Lin, B. Zhao, S. Zou, J. Guo, Z. Wei, L. Chen, Impact of viscous droplets on different wettable surfaces: Impact phenomena, the maximum spreading factor, spreading time and post-impact oscillation, J. Colloid Interface Sci. 516 (2018) 86–97.

[9] L. Liu, Y. Zhang, G. Cai, P.A. Tsai, High-speed dynamics and temperature variation during drop impact on a heated surface, Int. J. Heat Mass Transf. 189 (2022), 122710.

[10] J. Wu, J.J. Huang, W.W. Yan, Lattice Boltzmann investigation of droplets impact behaviors onto a solid substrate, Colloids Surf. A Physicochem. Eng. Asp. 484 (2015) 318–328.

[11] J. Philippi, P.-Y. Lagrée, A. Antkowiak, Drop impact on a solid surface: short-time self-similarity, J. Fluid Mech. 795 (2016) 96–135.

[12] H. Wang, C. Liu, H. Zhan, Y. Liu, Droplet asymmetric bouncing on inclined superhydrophobic surfaces, ACS Omega 4 (7) (2019) 12238–12243.

[13] S. LeClear, J. LeClear, K.-C. Abhijeet, W. Choi, Drop impact on inclined superhydrophobic surfaces, J. Colloid Interface Sci. 461 (2016) 114–121.

[14] M. Arogeti, E. Sher, T. Bar-Kohany, Drop impact on small targets with different target-to-drop diameters ratio, Chem. Eng. Sci. 193 (2019) 89–101.

[15] S. Ding, Z. Hu, L. Dai, X. Zhang, X. Wu, Droplet impact dynamics on single-pillar superhydrophobic surfaces, Phys. Fluids 33 (10) (2021), 102108.

[16] Y. Zhu, H.-R. Liu, K. Mu, P. Gao, H. Ding, X.-Y. Lu, Dynamics of drop impact onto a solid sphere: spreading and retraction, *J. Fluid Mech.* 824 (2017) R3.

[17] X. Liu, J. Min, X. Zhang, Dynamic behavior and maximum spreading of droplets impacting concave spheres, Phys. Fluids 32 (9) (2020), 092109.

[18] X. Liu, X. Zhang, Maximum spreading of droplets impacting spherical surfaces, Phys. Fluids 31 (2019), 092102.

[19] X. Liu, Y. Zhao, S. Chen, S. Shen, X. Zhao, Numerical research on the dynamic characteristics of a droplet impacting a hydrophobic tube, Phys. Fluids 29 (6) (2017), 062105.

[20] W. Zhao, Y. Zhang, W. Shang, Z. Wang, B. Xu, S. Jiang, Simulation of droplet impacting a square solid obstacle in microchannel with different wettability by using high density ratio pseudopotential multiple-relaxation-time (MRT) lattice Boltzmann method (LBM), Can. J. Phys. 97 (1) (2019) 93–113.

[21] Y.Q. Zu, Y.Y. Yan, Lattice Boltzmann method for modelling droplets on chemically heterogeneous and microstructured surfaces with large liquid–gas density ratio, IMA J. Appl. Math. 76 (5) (2011) 743–760.

[22] Y.Q. Zu, Y.Y. Yan, J.Q. Li, Z.W. Han, Wetting behaviours of a single droplet on biomimetic micro structured surfaces, J. Bionic Eng. 7 (2) (2010) 191–198.

[23] Y. Shen, et al., Bouncing dynamics of impact droplets on the convex superhydrophobic surfaces, Appl. Phys. Lett. 110 (22) (2017), 221601.

[24] Y. Liu, L. Moevius, X. Xu, T. Qian, J.M. Yeomans, Z. Wang, Pancake bouncing on superhydrophobic surfaces, Nat. Phys. 10 (7) (2014) 515–519.

[25] J. Luo, F. Chu, Z. Ni, J. Zhang, D. Wen, Dynamics of droplet impacting on a cone, Phys. Fluids 33 (11) (2021), 112116.

[26] K. Sun, M. Jia, T. Wang, Numerical investigation of head-on droplet collision with lattice Boltzmann method, Int. J. Heat Mass Transf. 58 (1) (2013) 260–275.

[27] L. Chen, Q. Kang, Y. Mu, Y.-L. He, W.-Q. Tao, A critical review of the pseudopotential multiphase lattice Boltzmann model: methods and applications, Int. J. Heat Mass Transf. 76 (2014) 210–236.

[28] F. Qin, A. Mazloomi Moqaddam, Q. Kang, D. Derome, J. Carmeliet, Entropic multiple-relaxation-time multirange pseudopotential lattice Boltzmann model for two-phase flow, Phys. Fluids 30 (3) (2018), 032104.

[29] W. Xiong, P. Cheng, 3D lattice Boltzmann simulation for a saturated liquid droplet at low Ohnesorge numbers impact and breakup on a solid surface surrounded by a saturated vapor, Comput. Fluids 168 (2018) 130–143.

[30] J.M. Gac, L. Gradoń, Lattice-Boltzmann modeling of collisions between droplets and particles, Colloids Surf. A Physicochem. Eng. Asp. 441 (2014) 831–836.

[31] Y.Y. Yan, Y.Q. Zu, A lattice Boltzmann method for incompressible two-phase flows on partial wetting surface with large density ratio, J. Comput. Phys. 227 (1) (2007) 763–775.

[32] S. Shen, F. Bi, Y. Guo, Simulation of droplets impact on curved surfaces with lattice Boltzmann method, Int. J. Heat Mass Transf. 55 (23) (2012) 6938–6943.

[33] A. Merdasi, S. Ebrahimi, A. Moosavi, M.B. Shafii, F. Kowsary, Simulation of a falling droplet in a vertical channel with rectangular obstacles, Eur. J. Mech. B. Fluids 68 (2018) 108–117.

[34] M. Bakhshan, M. Wörner, A. Dadvand, Simulation of droplet impingement on a rigid square obstacle in a microchannel using multiphase lattice Boltzmann method, Comput. Particle Mech. 8 (4) (2021) 973–991.

[35] S. Gong, P. Cheng, Numerical investigation of droplet motion and coalescence by an improved lattice Boltzmann model for phase transitions and multiphase flows, Comput. Fluids 53 (2012) 93–104.

[36] X. Shan, H. Chen, Lattice Boltzmann model for simulating flows with multiple phases and components, Phys. Rev. E, Stat. Phys. Plasmas Fluids Relat. Interdisciplinary Top. 47 (1993) 1815–1819.

[37] P. Yuan, L. Schaefer, A thermal lattice Boltzmann two-phase flow model and its application to heat transfer problems—Part 1. Theoretical foundation, J. Fluids Eng. 128 (1) (2005) 142–150.

[38] P.L. Bhatnagar, E.P. Gross, M. Krook, A model for collision processes in gases. I. Small amplitude processes in charged and neutral one-component systems, *Phys. Rev.* 94 (3) (1954) 511–525.

[39] C. Zhang, P. Cheng, W.J. Minkowycz, Lattice Boltzmann simulation of forced condensation flow on a horizontal cold surface in the presence of a non-condensable gas, Int. J. Heat Mass Transf. 115 (2017) 500–512.

[40] X. Shan, H. Chen, Lattice Boltzmann model for simulating flows with multiple phases and components, *Phys. Rev. E* 47 (3) (1993) 1815–1819.

[41] Q. Kang, D. Zhang, S. Chen, Displacement of a two-dimensional immiscible droplet in a channel, Phys. Fluids 14 (9) (2002) 3203–3214.

[42] P. Yuan, L. Schaefer, Equations of state in a lattice Boltzmann model, *Phys. Fluids* 18 (4) (2006) 042101.

[43] J. Zhang, H. Chen, Y. Zhou, G. Cao, Simulation on the process of single bubble floating and colliding oil droplet based on improved three-component pseudo-potential Boltzmann method, J. Pet. Sci. Eng. 198 (2021), 108119.

[44] S. Gong, P. Cheng, A lattice Boltzmann method for simulation of liquid–vapor phase-change heat transfer, Int. J. Heat Mass Transf. 55 (17) (2012) 4923–4927.

[45] C. Zhang, P. Cheng, Mesoscale simulations of boiling curves and boiling hysteresis under constant wall temperature and constant heat flux conditions, Int. J. Heat Mass Transf. 110 (2017) 319–329.

[46] A. Hu, L. Li, S. Chen, Q. Liao, J. Zeng, On equations of state in pseudo-potential multiphase lattice Boltzmann model with large density ratio, Int. J. Heat Mass Transf. 67 (2013) 159–163.

[47] Q. Li, K.H. Luo, Q.J. Kang, Q. Chen, Contact angles in the pseudopotential lattice Boltzmann modeling of wetting, *Phys. Rev. E* 90 (5) (2014) 053301.

[48] Q. Zou, X. He, On pressure and velocity flow boundary conditions and bounceback for the lattice Boltzmann BGK model, *Phys. Fluids* 9 (6) (1997).

[49] O. Filippova, D. Hanel, Grid refinement for lattice-BGK models, *J. Comput. Phys.* 147 (1) (1998) 219–228.

[50] C.K. Law, Recent advances in droplet vaporization and combustion, Prog. Energy Combust. Sci. 8 (3) (1982) 171–201.

[51] A.R. Rahmati, A. Zarareh, Application of a modified pseudopotential lattice Boltzmann model for simulation of splashing phenomenon, Eur. J. Mech. B. Fluids 70 (2018) 19–35.

[52] R. Ma, X. Zhou, B. Dong, W. Li, J. Gong, Simulation of impacting process of a saturated droplet upon inclined surfaces by lattice Boltzmann method, Int. J. Heat Fluid Flow 71 (2018) 1–12.

[53] D. Quéré, Leidenfrost dynamics, Annu. Rev. Fluid Mech. 45 (1) (2013) 197–215.